

Architected continuum mixed ionic and electronic conducting alloy negative electrode for fast-charging all-solid-state lithium batteries

Received: 27 March 2025

Accepted: 27 November 2025

Published online: 16 December 2025

Check for updates

Tao Liu^{1,2,8}, Youlong Sun^{2,3,4,8}, Yantao Wang^{2,8}, Shu Zhang², Yuchen Zhang^{2,4}, Shanmu Dong^{2,3,5} ✉, Jinzhi Wang², Chuanchuan Li², Lei Hu², Weijiang Xue⁶ ✉, Jiangwei Ju^{2,5}, Jun Ma^{2,5}, Bo Tang^{1,7} ✉ & Guanglei Cui^{1,2,3,4,5} ✉

All-solid-state lithium batteries for electric vehicles require high specific power, challenged in thick negative electrodes by fragile conducting networks during volume changes and dendrite growth at high currents. We propose an $\text{In}_{0.38}\text{Sn}_{0.33}\text{Bi}_{0.29}$ ternary alloy negative electrode creating a mixed ionic-electronic conducting continuum that overcomes these limitations. The stepwise formation of multiple phases with sufficient mechanical robustness during Li-alloying effectively stabilizes the ionic and electronic conducting percolation by relieving stress concentration and minimizing crack propagation. The unique reversibility of the multiple phase changes during lithiation/delithiation ensures stable cycling performance. The $\text{In}_{0.38}\text{Sn}_{0.33}\text{Bi}_{0.29}$ negative electrode exhibits a high capacity of $\sim 724 \text{ mAh g}^{-1}$ and a critical current density of 150 mA cm^{-2} at 5.0 mAh cm^{-2} . The $\text{In}_{0.38}\text{Sn}_{0.33}\text{Bi}_{0.29} \parallel \text{LiCoO}_2$ full cell with industry-level mass loading (6.49 mAh cm^{-2}) can retain 87.5% capacity over 1300 cycles at 4.0 C, delivering a jellyroll specific energy of 203.1 Wh kg^{-1} and 670.6 Wh L^{-1} at 5.0 C. The fast-charging capability is further validated by large-format pouch cells. The design principles can be extended to other negative electrode designs for solid-state batteries.

All-solid-state lithium batteries (ASSLBs) with high specific power (gravimetric and volumetric specific power in W kg^{-1} and W l^{-1} , respectively) offer great promise as the ideal batteries for electric vehicles and consumer products. However, the key bottleneck lies in the negative electrode materials, such as inefficient ion-electron transportation,

fragile conducting network, large volume change, and the lithium dendrite growth at high current densities^{1,2}. Although a lot of efforts have been devoted to address these issues in thin electrodes³⁻⁵, there still lack of effective strategies for industry-level thick ($>4 \text{ mAh cm}^{-2}$) negative electrodes, whereas the difficulty increases exponentially⁶.

¹College of Chemistry, Chemical Engineering and Materials Science, Shandong Normal University, Jinan, China. ²Qingdao Industrial Energy Storage Research Institute, Qingdao Institute of Bioenergy and Bioprocess Technology, Chinese Academy of Sciences, Qingdao, China. ³Qingdao New Energy Shandong Laboratory, Qingdao, China. ⁴Center of Materials Science and Optoelectronics Engineering, University of Chinese Academy of Sciences, Beijing, China. ⁵Shandong Energy Institute, Qingdao, China. ⁶Center for Advancing Materials Performance from the Nanoscale (CAMP-Nano), State Key Laboratory for Mechanical Behavior of Materials, Xi'an Jiaotong University, Xi'an, Shaanxi, China. ⁷Laoshan Laboratory, Qingdao, Shandong, China. ⁸These authors contributed equally: Tao Liu, Youlong Sun, Yantao Wang. ✉ e-mail: dongsm@qibebt.ac.cn; xuewj@xjtu.edu.cn; tangb@sdnu.edu.cn; cuiql@qibebt.ac.cn

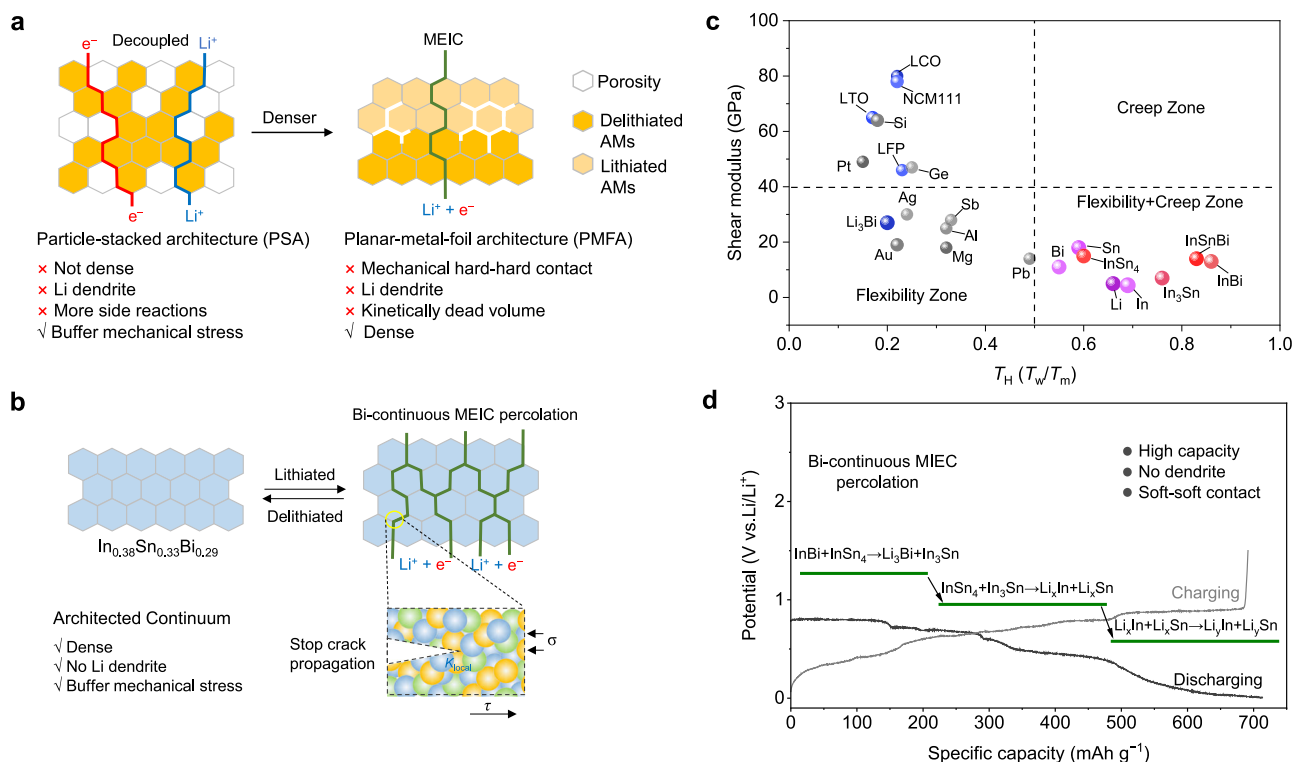


Fig. 1 | The design of the architected continuum alloy concept. **a** The conventional negative electrode architectures—PSA and PMFA with their advantages and disadvantages. **b** By adopting the advantages of the PSA and PMFA, the architected continuum alloy is designed, composed by multiple metal elements, featuring bi-continuous MIEC percolation and soft-soft contact to buffer the mechanical stress and to stop the crack-based degradation. **c** Deformation mechanism maps for

various materials at 25 °C (T_H is homologous temperature, where $T_H = T_w/T_m$, T_w =working temperature/melting temperature). The mechanical data and melting points of these materials are obtained from ref. 17 and the Material Project (materialsproject.org), accessed 2023-11-15. The In, Sn, and Bi were screened out with sufficient flexibility and creep behavior. **d** Schematic diagram of lithiation process and advantages of the designed InSnBi negative electrode.

To realize fast charging in a practical cell architecture with thick negative electrodes, it is crucial to create highly mixed ionic and electronic conducting (MIEC) percolations and to maintain intimate solid-solid contact at the nano-level^{7,8}. Generally, the prevailing negative electrode is based on a particle-stacked architecture (PSA, Fig. 1a), namely the mixture of active (like graphite, silicon, et al.) and inactive (conductive carbon and solid electrolyte) material particles compressed on Cu current collector⁹. This is a favorable architecture for fast charging because the movement of ions and electrons is largely decoupled (Fig. 1a) with nano-scale sufficient contact between the ionic and electronic percolations¹⁰. The mechanically soft sulfide-based solid electrolyte (SE) could buffer the mechanical stress and deform plastically to maintain close physical contact. However, this design exhibits insufficient specific energy, and conversion reactions suffer from the unstable three-phase boundaries among the active material, carbon, and solid electrolyte (SE), adversely affecting the cycling stability of negative electrodes with large volume change^{11,12}. Moreover, another type of negative electrodes, based on a planar-metal-foil architecture (PMFA, like the Li/Al/In-metal, Fig. 1a), has its volumetric advantage compared to the PSA, because it contains no porosity and other inactive components¹³. Ideal PMFA negative electrodes must function as mixed electronic and ionic conductors, maintaining intimate solid-solid contact throughout the lithiation/delithiation process. Although solid-electrolyte interface (SEI) could still be formed between the negative electrode and the SE, the volume change in ASSLBs tends to be a more mechanical behavior compared to liquid electrolyte-based batteries, as the accompanied chemical behavior (i.e., dissolution) can be eliminated. However, for PMFA negative electrodes, it is challenging to maintain the MIEC percolation integrity under large fluctuating mechanical stresses induced by cycling.

In a PMFA negative electrode, the grain boundary (GB) region often allows faster Li-atom movement than the bulk¹⁴, inducing alloy phase transformations and volume expansion along the diffusion pathway. Upon fast charging, local stress concentrations (K_{local}) are easily built up thermodynamically by the large driving force from the overpotential and structurally by the heterogeneous Li alloying¹⁵. If the potentially huge K_{local} is not relieved in a timely manner, it would initiate crack deformation, crack propagation, and porosity, which could not be accommodated by the hard-hard contact between the metal particles and their lithiated products. In this scenario, more and more dead volume is generated that is kinetically unavailable at high rates, eventually falling off from the MIEC percolations and thus hurting the fast charging capability¹⁶. This crack-induced degradation mode is especially true when the metal is lithiated and loses most of its ductility. A possible strategy to solve these electrochemically-generated mechanical issues in the PMFA negative electrode to facilitate fast-charging capability is to rationally design the compositions and microstructures of the PMF negative electrode, but it still remains unexplored.

Here, unlike previous works that employ single-phase alloy or multi-phase alloy negative electrodes^{17–19}, our approach precisely controls the ratio of three metallic elements, creating an architected continuum intermetallic compound negative electrode (Fig. 1b) that synergistically incorporates the advantages of both the PSA and PMFA. The core of this work is to design an energy-dense PMFA alloy (Fig. 1b) with: (1) soft phases to relieve mechanical stress; (2) the formation of bi-continuous highly conductive MIEC phases; and (3) resistance to Li dendrite formation at high current densities. To meet these multifunctional requirements, an alloy composed of multiple elements with a low eutectic point is preferable. From a mechanical view, we first

screened “soft” metals based on the homologous temperature ($T_H = \text{working temperature}/\text{melting temperature}$) and shear modulus in Fig. 1c since the metals with $T_H > 0.5$ exhibits significant creep behavior under applied external stress²⁰. In, Sn, Bi, and their alloys with low melt points show the highest T_H and soft characteristics (shear modulus < 40 MPa). Among these elements, Bi exhibits the highest lithiation potential (-0.75 V vs. Li/Li⁺), and its lithiation product Li₃Bi possesses the highest ionic conductivity, thereby enhancing the ion transport of lithiated electrode and suppressing Li dendrite formation. In and Sn, with their lower potentials and higher capacities, contribute to maximizing the overall specific capacity. The incremental lithiation of Li₃Bi, Li_xIn, and Li_ySn leads to continuously changing MIEC percolation network (Fig. 1d). Based on this understanding, a carefully tailored ternary alloy In_{0.38}Sn_{0.33}Bi_{0.29}, composed of 76% InBi and 24% InSn₄ ((InSn₄)_{0.24}(InBi)_{0.76}, abbreviated as InSnBi), has been developed. This alloy demonstrates a high specific capacity of 724 mAh g⁻¹, a low working potential of 0.47 V vs. Li/Li⁺, and a high critical current density (CCD) of up to 150 mA cm⁻²/5.0 mAh cm⁻² at 30 °C. With Li₆PS₃Cl (LiPSCl) as the SE, the InSnBi||LiCoO₂ cell demonstrated a jellyroll specific energy of 278.4 Wh kg⁻¹ (919.5 Wh L⁻¹) at 0.2 C, retaining 73.6% and 72.0% of its specific energy at 5.0 C and 6.0 C, respectively. The full cell exhibited a remarkable specific power of up to 1545.3 W kg⁻¹ (5103.8 W L⁻¹), rivaling that of supercapacitors. This architecture continuum alloy concept presents a significant milestone in negative electrode design for fast-charging and high-power-density ASSLBs.

Results and discussion

The design of the InSnBi negative electrode

The interfacial stability and mechanical properties of electrodes play a pivotal role in electrochemical performances, especially for alloy-type negative electrodes that experience large volume changes during (de) lithiation. In classical mechanics, a material with homologous temperature ($T_H = T_w/T_m$, T_w and T_m are working temperature and melting temperature, respectively) > 0.5²¹ would undergo significant creep and shape changes through self-diffusion in response to applied external stress below yield strength, causing polycrystalline solids to behave like viscous fluids at the macroscopic level. These characteristics effectively leverage the stress-driven creep and flexibility to facilitate interfacial contact and relieve stress, improving the contact between electronic and ionic percolations. Besides the shear modulus in Fig. 1c, we further evaluate the mechanical properties of the InSnBi alloy and its lithiated products by nanoindentation. Plastic deformation characteristics are observed from the nanoindentation load-displacement curves (Supplementary Fig. 1a, b), from which the hardness values were deduced. The hardness values of the InSnBi alloy (0.31 GPa) and lithiated products including Li₃Bi (0.71 GPa), In₃Sn (0.05 GPa), Li-In (0.26 GPa), and Li-Sn (0.51 GPa) are even much lower than the LiPSCl (1.93 GPa), which is also confirmed by the comparison of the hardness between the Li_xInSnBi at different lithiation states and the LiPSCl (Supplementary Fig. 1c).

In order to identify the optimal composition, we explored several ternary alloys composed of In, Sn, and Bi according to the critical current density (CCD) including In_{0.38}Sn_{0.33}Bi_{0.29}, In_{0.48}Sn_{0.32}Bi_{0.20}, In_{0.60}Sn_{0.25}Bi_{0.15}, and In_{0.75}Sn_{0.15}Bi_{0.10} (Supplementary Fig. 2). Among them, In_{0.38}Sn_{0.33}Bi_{0.29} was chosen for its highest CCD with a melting point of approximately 85 °C (Fig. 2a). Notably, the melting point of lithiated InSnBi exceeds 120 °C (Supplementary Fig. 3), effectively eliminating the risk of negative electrode melting during fast charging. Unlike the multiple steps required to manufacture conventional particle-stacked electrodes²², InSnBi foil can be easily fabricated by casting its molten form onto a copper collector in air (Fig. 2b and Supplementary Fig. 4). The InSnBi alloy's perfectly balanced rigidity and flexibility make it suitable for fabricating free-standing or thin electrodes (Fig. 2c and Supplementary Fig. 5). Interestingly, the InSnBi alloy consists of two

phases, InBi and InSn₄, as revealed by X-ray diffraction (XRD) results (Fig. 2d) and high-resolution transmission electron microscopy (Supplementary Fig. 6). The presence of In-Sn and In-Bi bonds in the InSnBi alloy is confirmed by a series of synchrotron-based techniques (Supplementary Fig. 7), while no In-In scattering (at -2.98 Å) is detected in the extended X-ray absorption fine structure (FT-EXAFS) shown in Fig. 2e. The InBi and InSn₄ phases are uniformly mixed at nano to submicron scale, forming a three-dimensional interconnected network (Fig. 2g). This phase composition and its spatial distribution characteristics provide the foundation for favorable MIEC percolation with high mechanical stability, enabling the alloy to accommodate the large fluctuating mechanical stresses generated during alloying and dealloying with Li.

As depicted in Fig. 2f, the InSnBi negative electrode exhibits an initial discharge specific capacity of 713 mAh g⁻¹ (theoretical value: 724 mAh g⁻¹) with a working potential of 0.47 V versus Li/Li⁺, indicating its potential suitability for high-energy batteries. Utilizing the InSnBi negative electrode paired with an NCM811 positive electrode, the estimated cell-level specific energy significantly surpasses that of Li₄Ti₅O₁₂||NCM811 and graphite||NCM811 full cells (Supplementary Fig. 8), even exceeding 400 Wh kg⁻¹ at a positive electrode loading of 35 mg cm⁻². Furthermore, the volumetric capacity of the InSnBi (1998 mAh cm⁻³) is 2.6–3.4 times higher than that of typical PSA negative electrodes like graphite (781 mAh cm⁻³) and Li₄Ti₅O₁₂ (598 mAh cm⁻³), making it advantageous for achieving high volumetric specific energy.

Interface compatibility and stability

To evaluate the InSnBi's ability for fast charging in ASSLBs, we investigated the critical current density (CCD) of Li-InSnBi||LiPSCl||Li-InSnBi symmetric cells at a fixed capacity of 5.0 mAh cm⁻² (Fig. 3a, Supplementary Fig. 9, and Supplementary Note 1). Notably, the CCD of the Li-InSnBi negative electrode (more than 75% lithiation degree) can reach up to 150 mA cm⁻² at 30 °C, which is one of the highest levels among the state-of-the-art negative electrodes (Supplementary Fig. 10). Moreover, the CCD of the Li-InSnBi negative electrode can be further increased to more than 200 mA cm⁻² at 60 °C (Supplementary Fig. 11).

To evaluate the long-term stability of InSnBi, Li-InSnBi||LiPSCl||Li-InSnBi symmetric cells were cycled at 100 mA cm⁻²/5 mAh cm⁻². As shown in Fig. 3b and Supplementary Fig. 12, the cell can survive for over 5500 cycles (550 h). Electrochemical impedance spectroscopy (EIS, Supplementary Fig. 13) results reveal that the interfacial impedance remains stable during prolonged cycling. Additionally, our InSnBi negative electrode exhibited high performance in the Li-In||Li-InSnBi half-cell configuration, achieving an average Coulombic efficiency of 99.92% over 500 cycles (Supplementary Fig. 14). The EIS results and corresponding distribution of relaxation times (DRT) of the InSnBi||LiCoO₂ cell confirm stable contact impedance (R_c) during long-term cycling (Supplementary Fig. 15), further indicating stable chemo-mechanical compatibility between InSnBi and LiPSCl during cycling.

The 3D morphology of the In||LiCoO₂ and In_{0.38}Sn_{0.33}Bi_{0.29}||LiCoO₂ cells cycled at 8.2 mA cm⁻² was acquired by X-ray computed tomography (XCT, Fig. 3c, d). In contrast to the In negative electrode with severe Li-In dendritic growth (Fig. 3c, Supplementary Note 2), no dendrite formation was observed in our InSnBi negative electrode (Fig. 3d). Raman analysis (Fig. 3e) demonstrates that the interfacial reaction between In-metal and LiPSCl produces In₂S₃, which has been identified as the primary cause of Li-In dendrite formation²³. Both Raman mapping (Supplementary Fig. 16) and X-ray photoelectron spectroscopy (XPS, Supplementary Fig. 17) results suggest the suppressed interfacial reactions between InSnBi (and lithiated InSnBi) and LiPSCl, which can be further verified by the First-principles thermodynamic calculations (Fig. 3f)²⁴. Additionally, Raman spectroscopic analysis of LiPSCl after cycling reveals a uniform distribution of PS₄³⁻

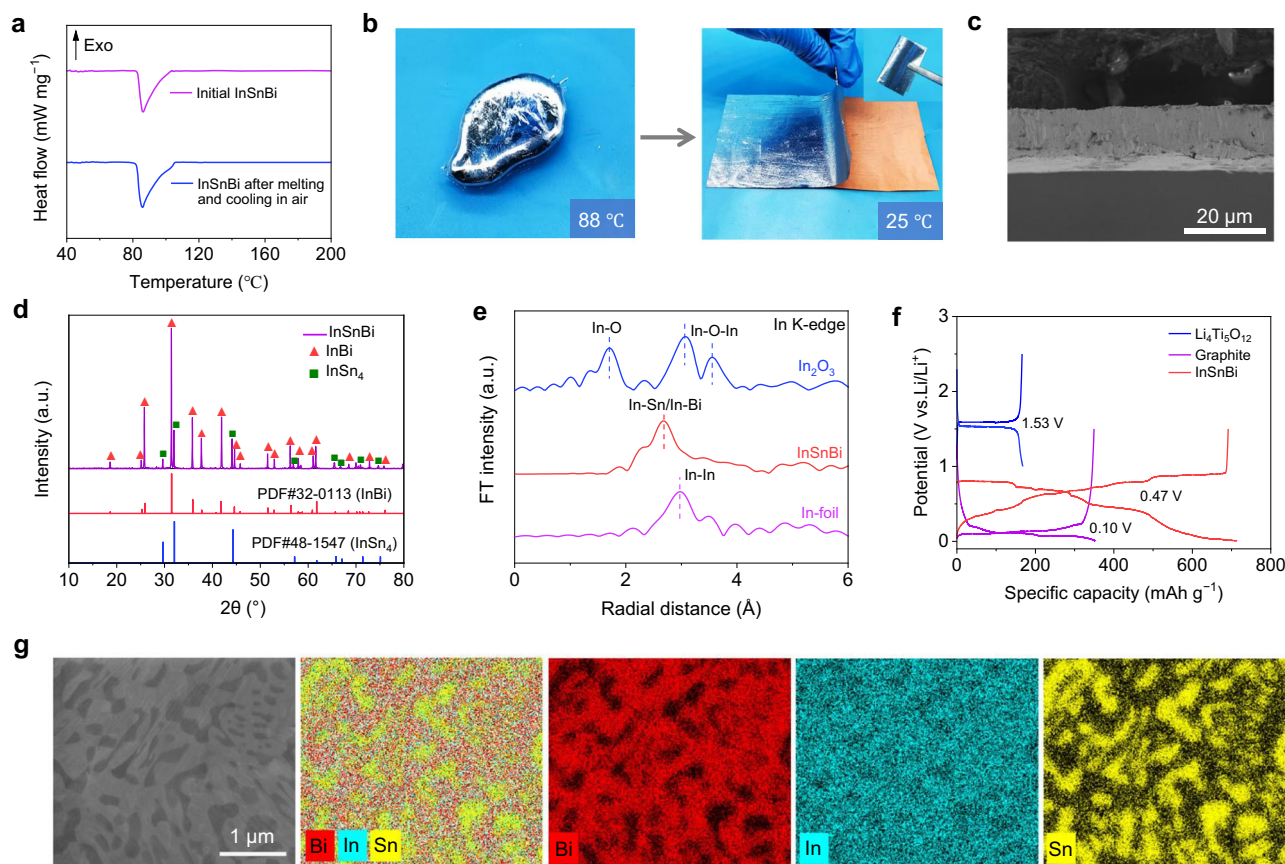


Fig. 2 | Characterizations of the InSnBi. **a** DSC heating profiles of the initial InSnBi and the InSnBi after melting and cooling in air. **b** Digital images of the InSnBi fabrication process. **c** Cross-sectional scanning electron microscope (SEM) image of the free-standing InSnBi. **d** XRD patterns, and **e** EXAFS spectra of In K-edge for

the InSnBi. **f** Voltage profiles of the graphite, InSnBi, and $\text{Li}_4\text{Ti}_5\text{O}_{12}$ negative electrodes evaluated by half cells with liquid electrolytes at 0.15 C. **g** SEM image and EDS elemental mappings of the InSnBi.

tetrahedral structures (425 cm^{-1}) (Fig. 3g), while Li_2S (372 cm^{-1}) exhibits relatively weak Raman spectral intensity across the entire electrode surface (Supplementary Fig. 18). These observations indicate that the majority of LiPSCl in contact with the lithiated InSnBi negative electrode maintains its structural stability during cycling. These findings demonstrate that both pristine InSnBi and lithiated InSnBi exhibit stable compatibility with LiPSCl.

Electrochemical performance

To evaluate the rate performance of the InSnBi negative electrode in ASSLBs, prelithiated InSnBi negative electrodes were coupled with various positive electrodes (Supplementary Note 3 and Supplementary Fig. 19). The InSnBi || LiCoO₂ cell exhibits reversible capacities of 159.5, 147.3, 127.8, 110.1, 95.4, 85.3, and 72.8 mAh g⁻¹ at rates of 2.5 C, 5 C, 10 C, 20 C, 30 C, 40 C, and 50 C, respectively (Fig. 4a and Supplementary Fig. 20). Specifically, the InSnBi || LiCoO₂ cell maintains 66.7% and 44.1% of its capacity at 20 C and 50 C, respectively (Fig. 4b). In contrast, the cell with the Mix-InSnBi negative electrode (Mix-InSnBi refers to a simple physical mixture of In, Sn, and Bi powders in an atomic ratio of 38:33:29) exhibits significantly poorer rate performance, retaining only 35.0% and 7.4% of its capacity at 20 C and 50 C, respectively (Supplementary Fig. 21). Furthermore, when the LiCoO₂ loading was increased to 21.0 mg cm⁻², the InSnBi || LiCoO₂ cell still maintains its 63.5% and 49.4% capacities at 5 and 10 C, respectively (Supplementary Fig. 22). Meanwhile, the InSnBi || NCM83 cell also demonstrates high-rate performance ranging from 0.2 to 10 C (Supplementary Fig. 23), with capacities of 211.8, 192.5, 173.3, 150.1, 133.7, 110.5, and 72.8 mAh g⁻¹ at rates of 0.2 C, 0.5 C, 1.0 C, 2.0 C, 3.0 C, 5.0 C, and 10 C, respectively.

Various stack pressures were employed to assess the effect of pressure on the capacity of the InSnBi negative electrode (Fig. 4c). Only 20 MPa is required for the InSnBi || LiCoO₂ cell to achieve the highest capacity, while 70 MPa is needed for the Mix-InSnBi || LiCoO₂ cell. During 10 C operation, the InSnBi || LiCoO₂ cell shows a capacity retention of 82.2% with an average Coulombic efficiency (CE) of 99.96% over 3000 cycles (Supplementary Fig. 24). Even under industry-level parameters including low negative/positive capacity (N/P) ratio of 1.5 and high areal capacity of 6.49 mAh cm⁻², the InSnBi || LiCoO₂ full-cell still displays a high initial capacity of 4.58 mAh cm⁻² at 4.0 C and sustains a capacity retention of 87.5% along with an average CE of 99.93% after cycling at 4 C for 1300 cycles (Fig. 4d). In contrast, the full cell fabricated with Mix-InSnBi, and the compositionally distinct In_{0.60}Sn_{0.20}Bi_{0.20}, In_{0.20}Sn_{0.60}Bi_{0.20}, and In_{0.20}Sn_{0.20}Bi_{0.60} negative electrodes exhibit much lower capacity retention (less than 50%) after extended cycling (Supplementary Fig. 25). Furthermore, the InSnBi || LiCoO₂ cell could also maintain a desirable wide-temperature performance from -20 to 60 °C (Fig. 4e).

The significantly better electrochemical performance of the PMFA-type InSnBi negative electrode compared to the Mix-InSnBi indicates good interfacial contact during cycling, which guides us to characterize the contact between the InSnBi negative electrode and LiPSCl. As shown in Fig. 4f-h, the InSnBi electrode retains its structural integrity without pulverization or void formation and maintains tight contact with LiPSCl, despite significant volume expansion and contraction. Furthermore, the stack pressure fluctuation monitored during cycling remains consistently within a very narrow range (Supplementary Fig. 26), indicating the high structure stability and

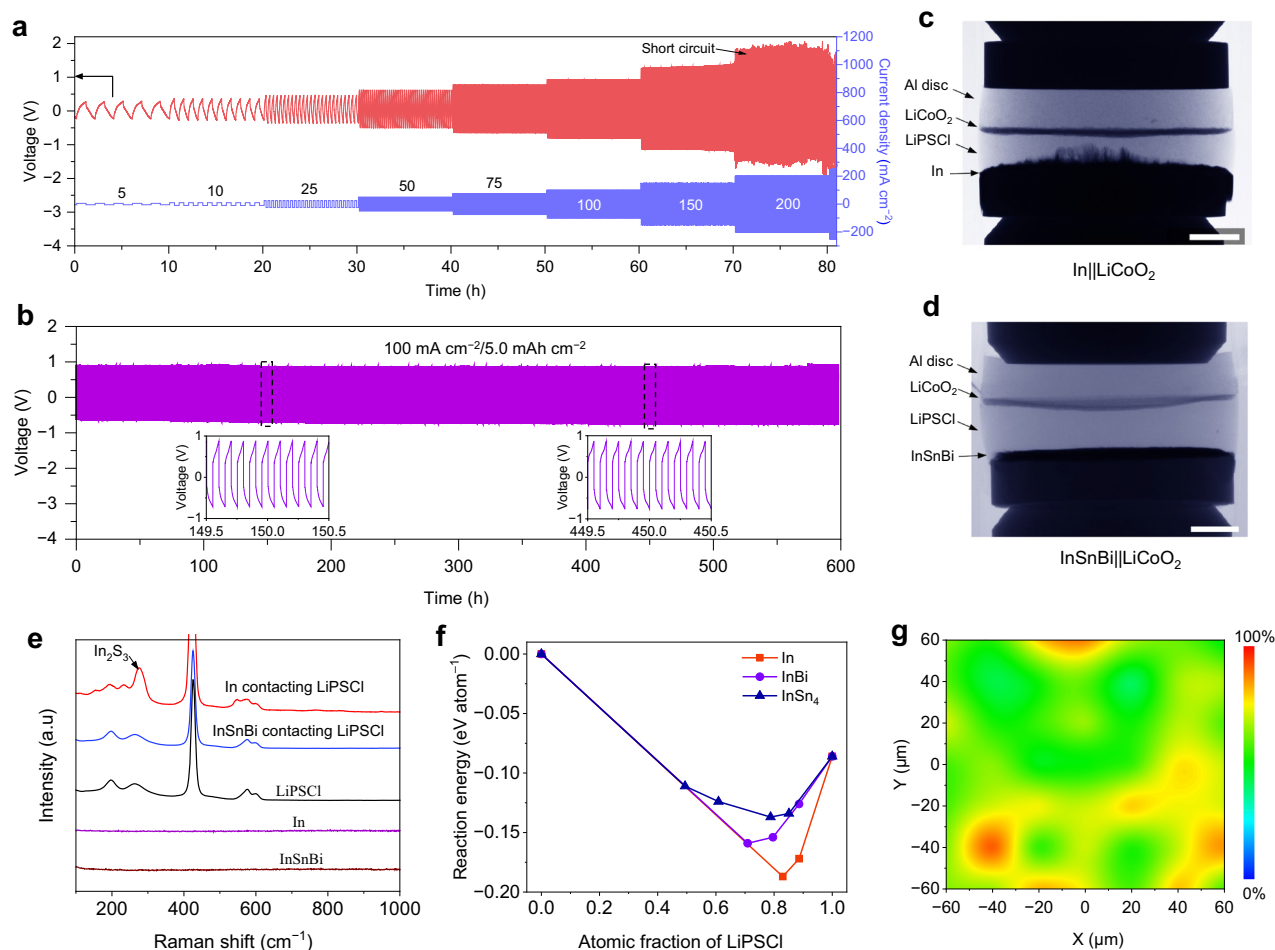


Fig. 3 | Electrochemical performance of the InSnBi at 30 °C. **a** The CCD of the Li-InSnBi|LiPSCI|Li-InSnBi symmetric cell measured from 5.0 to 250 mA cm⁻² with a fixed capacity of 5.0 mAh cm⁻². **b** Voltage profiles of symmetric Li-InSnBi cells cycled at 100 mA cm⁻². XCT images of cycled negative electrodes (in the lithiated state) at 8.2 mA cm⁻² over 20 cycles, **c** In negative electrode, **d** In_{0.38}Sn_{0.33}Bi_{0.29}

negative electrode. Scale bars in **c**, **d**: 400 μm. **e** Raman spectra of fresh In foil and InSnBi foil in contact with LiPSCI for 48 h. **f** Calculated mutual reaction energies between various components and LiPSCI. **g** Raman mapping image of 425 cm⁻¹ intensity of LiPSCI surface after 10 cycles (120 × 120 μm). 100% corresponds to the peak intensity of pure LiPSCI, while 0% indicates the absence of any peak intensity.

electrochemical reversibility of the InSnBi electrode throughout cycling. The structure integrity and stability is quite desirable for thick negative electrodes, which can be reflected by the cell with high mass loadings (Supplementary Fig. 27). The InSnBi||NCM83 cell with a positive electrode loading of 62.7 mg cm⁻² delivers a high initial capacity of 8.66 mAh cm⁻² at 0.3 C and retains a capacity of 6.47 mAh cm⁻² over 150 cycles. The cell constructed by LiCoO₂ (94.9 mg cm⁻²) and InSnBi shows a high initial capacity of 12.0 mAh cm⁻² at 0.3 C with high capacity retentions of 83.3% and 71.7% after 200 and 350 cycles, respectively. This cycling performance represents one of the most advanced levels under such high positive electrode loadings^{25,26}.

Fast ionic and electronic transport

To investigate the MIEC mechanism of the InSnBi negative electrode, we measured its ionic and electronic conductivities at various lithiation states at 25 °C (Supplementary Fig. 28)²⁷. The Li⁺ ionic conductivities of Li_xInSnBi range from 0.32 to 1.12 mS cm⁻¹ (Supplementary Fig. 29), comparable to those of solid sulfide electrolytes²⁸. These conductivities increase to 0.56–1.72 mS cm⁻¹ at 40 °C and further to 1.07–2.91 mS cm⁻¹ at 60 °C (Supplementary Fig. 29). The ionic conductivity increases with the degree of lithiation, significantly reducing the risk of lithium dendrite formation at low potentials. The electronic conductivity of Li_xInSnBi exceeds 180 S cm⁻¹,

substantially higher than that of most conductive carbon materials⁸. Moreover, the co-migration of ions and electrons within the same medium in the Li_xInSnBi electrode reduces the tortuosity of charge transport pathways, enhancing the efficiency of ionic and electronic transport.

The room-temperature Li⁺ diffusion coefficient of Li_xInSnBi is notably higher than 1 × 10⁻¹² m² s⁻¹ (Supplementary Fig. 30), improving that of conventional negative electrodes such as graphite²⁹, Li-metal³⁰, Li₄Ti₅O₁₂³¹, and Li-Si³². It is also comparable to that of the fast-charging Li_{6.3}Nb₁₆W₅O₅₅ negative electrode³³ and solid sulfide electrolytes^{34,35}. Combining the relationship between diffusion coefficient and diffusion lengths (Supplementary Table 1) reveals that the Li⁺ diffusion coefficient of Li_xInSnBi significantly exceeds the requirements for both 10 C and 25 C rate performance at a commercial-level areal capacity of 4 mAh cm⁻².

In situ XRD analysis was conducted to investigate the lithiation and delithiation processes (Fig. 5a). The initial InSnBi only consists of InBi (25.8°, 31.5°, and 35.8°) and InSn₄ (29.7°, 32.1°, and 44.3°). During the initial lithiation process, three distinct peaks at 22.9°, 26.5°, and 37.8° appear, corresponding to Li₃Bi, indicating that the Bi atoms are lithiated first due to the high lithiation potential (0.75 V vs. Li/Li⁺). As lithiation progresses, the Li₃Bi peaks intensify, while the InBi and InSn₄ peaks gradually diminish. Concurrently, peaks at 32.9° and 36.6° corresponding to In₃Sn emerge and intensify. These observations suggest

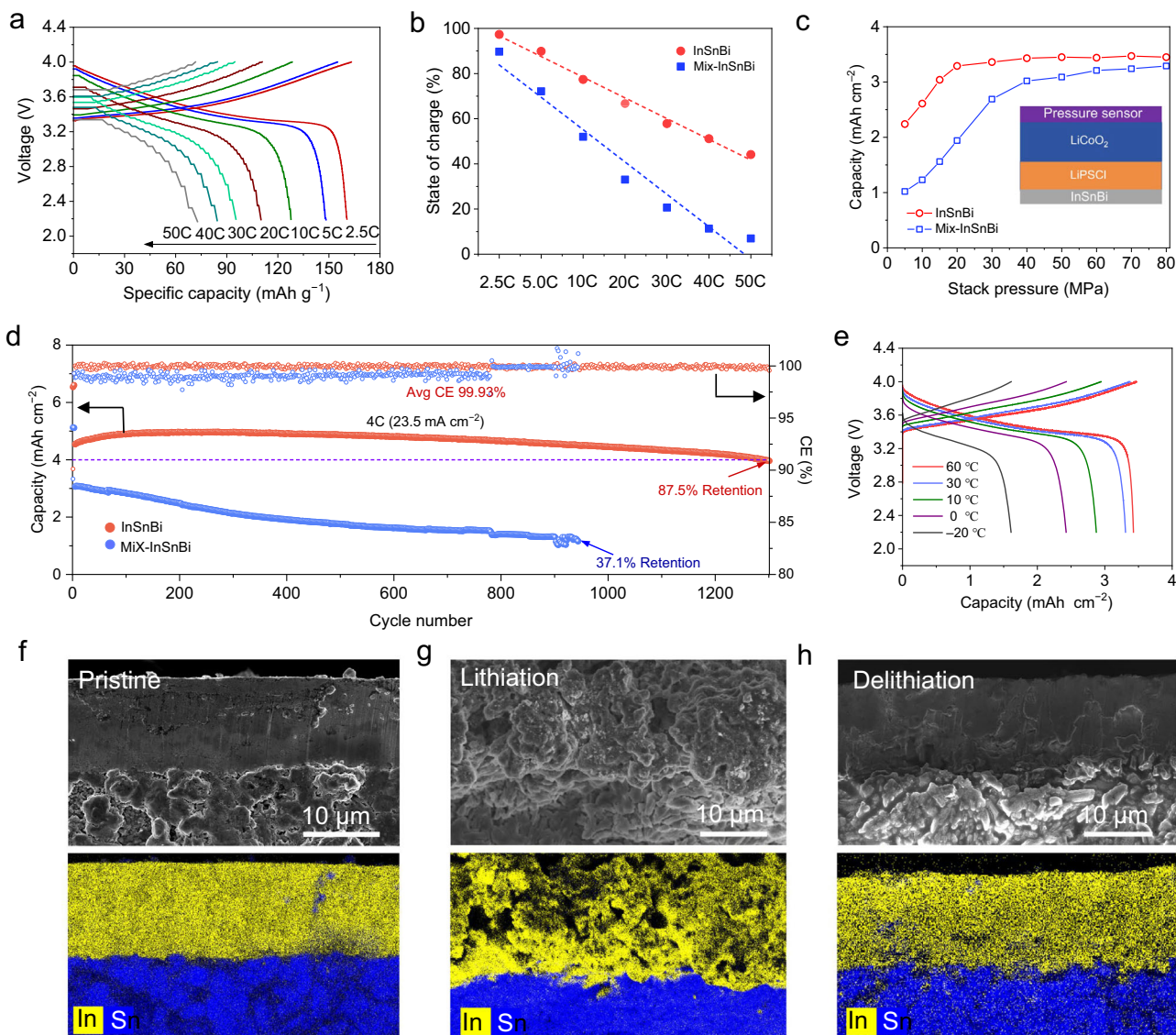


Fig. 4 | Electrochemical performance of InSnBi negative electrodes at 60 °C. **a** Rate performance of InSnBi || LiCoO₂ cell with a positive electrode loading of 7.8 mg cm⁻². **b** positive electrode capacity of different samples at various rates. **c** Effect of cell stack pressure on capacity performance. **d** Cycling performance of the InSnBi || LiCoO₂ cell with a positive electrode loading of 39.7 mg cm⁻² at 4 C.

e Performance of the InSnBi || LiCoO₂ cell at 0.1 C at various temperatures. Cross-sectional SEM and EDS images of the InSnBi negative electrode during the lithiation/delithiation process: **f** pristine state, **g** lithiation state (after 5 cycles), and **(h)** delithiation state (after 5 cycles). (LiCoO₂ based on 1 C = 145 mAh g⁻¹).

that In atoms detach from InBi and react with InSn₄, forming In₃Sn during the Bi lithiation process. As lithiation continues, In₃Sn/InSn₄ gradually transforms into a mixture of amorphous Li-In and Li-Sn (Fig. 5e, Supplementary Fig. 31). Notably, after initial lithiation of Bi atoms, the subsequent lithiation of In and Sn atoms proceeds synergistically, without a distinguishable sequential order. This concurrent lithiation mechanism interrupts the crystallization process of Li-In and Li-Sn phases. Notably, all these lithiation processes are fully reversible. The Li₃Bi, Li-In, and Li-Sn phases can recover to their original InBi and InSn₄ phases during delithiation (Supplementary Fig. 32). The three-dimensional ion channel network of Li₃Bi, which features the flattest energy landscape with the lowest Li⁺ migration barrier (Fig. 5b, Supplementary Data 1), results in high ionic conductivity (2.33 mS cm⁻¹, Supplementary Fig. 33), as previously reported³⁶. Notably, Li₃Bi remains the dominant phase throughout the cycling process due to its high lithiation potential, making it an ideal Li⁺ conducting backbone for InSnBi (Fig. 5c and d). Furthermore, this heterogeneous structure, where crystalline Li₃Bi is embedded within amorphous Li-In/Li-Sn

compounds, enhances ion transport at both the bulk and interfacial levels through nanoscale interface effects¹¹.

The Li_xInSnBi alloy maintains an intact morphology without notable cracks, ensuring tight solid-solid contact between active materials (Supplementary Fig. 34). Density functional theory (DFT) simulations were performed to investigate Li⁺ diffusion barriers (Fig. 5g, h, Supplementary Data 1) across grain boundaries. The activation energy for Li⁺ diffusion across Li₃Bi (110)/Li₇Sn₂ (amorphous) and Li₃Bi (110)/Li₁₃Sn₃ (amorphous) interfaces is much lower than that across Li₃Bi (110)/Li₇Sn₂ (010) and Li₃Bi (110)/Li₁₃Sn₃ (110) grain boundaries, indicating that the grain-boundary-free characteristics of amorphous Li-Sn and Li-In facilitate Li⁺ migration between active particles³⁷. Furthermore, ab initio molecular dynamics (AIMD) simulations (Supplementary Fig. 35, Supplementary Data 1) demonstrate that amorphous Li-In and Li-Sn phases exhibit higher lithium-ion conduction percolation compared to crystalline Li₇Sn₂ and Li₁₃Sn₃, attributed to the open structure of their glassy networks and isotropic ionic conduction. These results reveal that the unique

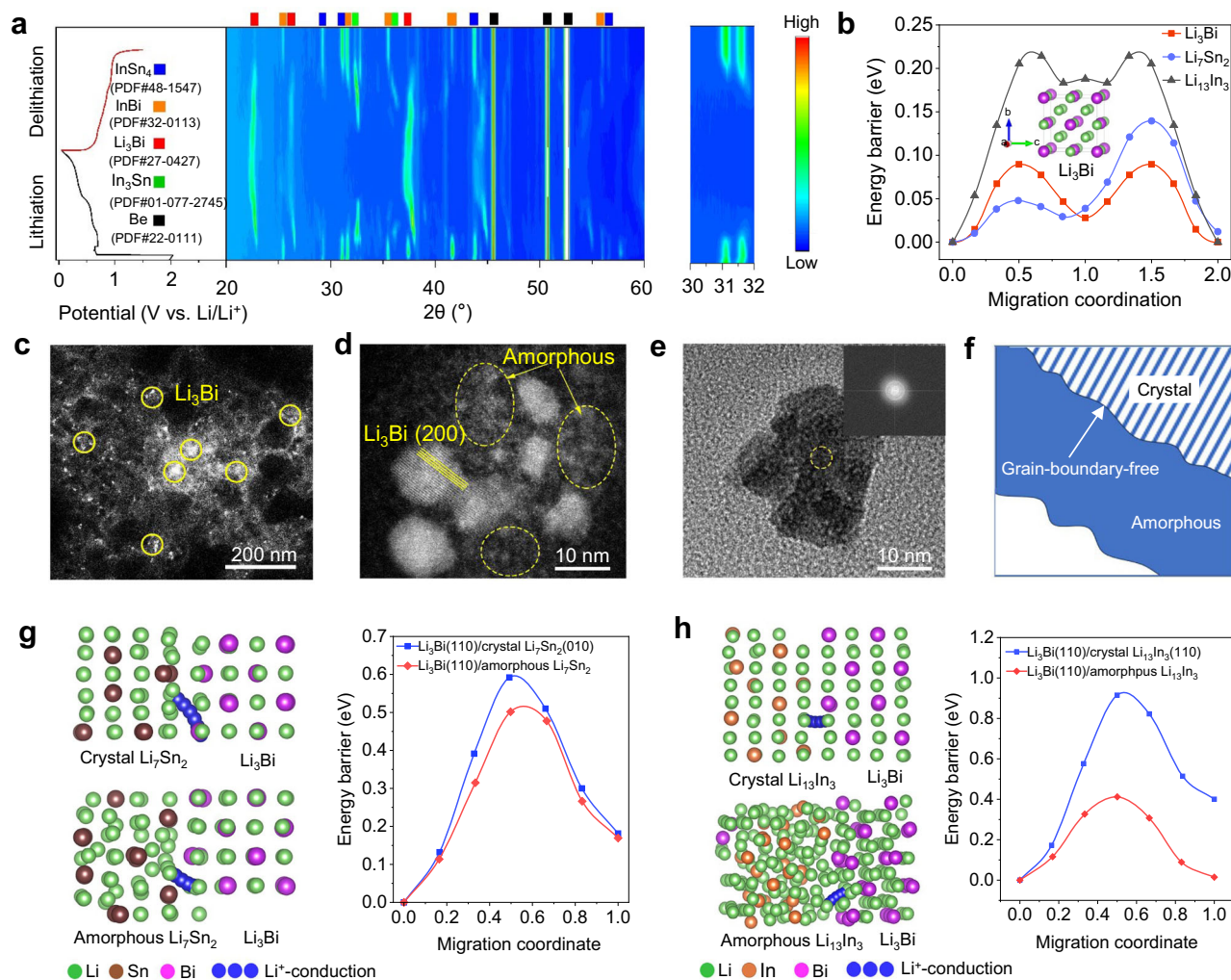


Fig. 5 | Fast-charging mechanism of the InSnBi negative electrode. **a** In situ XRD analysis of the InSnBi electrode cycled at a rate of 0.1 C at room temperature. **b** Li^+ diffusion energy barrier of bulk Li_3Bi , Li_7Sn_2 and $\text{Li}_{13}\text{In}_3$. **c–e** cryo-TEM images with different magnifications and the corresponding FFT pattern (after 5 cycles).

f Schematics of interphases between crystals and amorphous materials. Li^+ transport pathways and corresponding diffusion energies across crystalline-amorphous interfaces and between crystalline phases: **g** Li_3Bi (110)/ Li_7Sn_2 (010) and Li_3Bi (110)/amorphous Li_7Sn_2 , **h** Li_3Bi (110)/ $\text{Li}_{13}\text{In}_3$ (110) and Li_3Bi (110)/amorphous $\text{Li}_{13}\text{In}_3$.

crystal/amorphous structure in lithiated InSnBi not only facilitates intact solid-solid contact but also significantly reduces grain boundary resistance.

Practical application in full-cells

Considering the requirements for practical ASSLBs, the InSnBi||LiCoO₂ full-cell was assembled with a high active loading (~21.0 mg cm⁻²), a thin solid electrolyte (41.5 μm), and an N/P ratio of 1.3 (Fig. 6a and Supplementary Fig. 36). The full-cell delivers a capacity of 3.46 mAh cm⁻² at 0.2 C and maintains 94.9%, 89.8%, 83.1%, 78.8%, 75.7%, 73.6%, and 72.0% of the initial capacity within 111, 53, 25, 16, 12, 9.5, and 8 min (0.5, 1.0, 2.0, 3.0, 4.0, 5.0, and 6.0 C), respectively (Fig. 6b and Supplementary Fig. 37). Taking into account the weights of positive electrode (LiCoO₂, VGCF, LiPSCI), negative electrode (InSnBi), and the solid-state electrolyte film (Supplementary Table 2), the InSnBi||LiCoO₂ cell demonstrated a jellyroll specific energy of 278.4 Wh kg⁻¹ (919.5 Wh L⁻¹) at 0.2 C. More importantly, the full cell maintained a specific energy of 203.1 Wh kg⁻¹ (670.6 Wh L⁻¹) within a 9.5-min charging period (5 C), demonstrating the fast-charging capability of the InSnBi negative electrode under practical conditions. Additionally, the InSnBi||LiCoO₂ full-cell demonstrated high jellyroll specific power, up to 1545.3 W kg⁻¹ at 6.0 C, which are much higher than those of the state-of-the-art ASSLBs (Fig. 6c, Supplementary

Fig. 38, and Supplementary Table 3)^{9,25,36,38–42}. It is noteworthy that the jellyroll specific energy of the cells can be increased to 297.2 Wh kg⁻¹ (1053.7 Wh L⁻¹) by reducing the solid electrolyte film to 25 μm. Additionally, at 30 °C, the InSnBi||NCM83 full-cell exhibited a specific energy of 314.5 Wh kg⁻¹ at 0.2 C (Supplementary Table 4), while the InSnBi||LiCoO₂ full-cell delivered a specific energy of 243.4 Wh kg⁻¹ at 0.2 C and maintained a high rate performance from 0.2 to 5.0 C (Supplementary Fig. 39).

A single-layer InSnBi||LiCoO₂ pouch cell (3.5 cm × 5.0 cm in dimension) with 19.8 mg cm⁻² LiCoO₂ maintains a capacity retention of 90.4% over 650 cycles at 4.0 C, even under lower pressure applied to the pouch cell, confirming its viability for practical application (Fig. 6d). A comparison of the performance of our InSnBi negative electrode with other available negative electrode materials and state-of-the-art fast-charging LIBs is presented in Fig. 6e (Supplementary Table 5). In comparison to previous works on solid-state batteries (based on Si and Li-In negative electrodes)^{36,43}, high-energy-density batteries (based on Si and Li-metal negative electrodes)^{44,45}, and fast-charging batteries (using LTO and graphite negative electrodes)^{3,4,46}, our InSnBi||LiCoO₂ cell can simultaneously realize fast-charging capability (<10 min) and high specific energy (> 200 Wh kg⁻¹), even comparable to previous fast-charging liquid batteries with the rapid thermal modulation⁴. Our full-cell

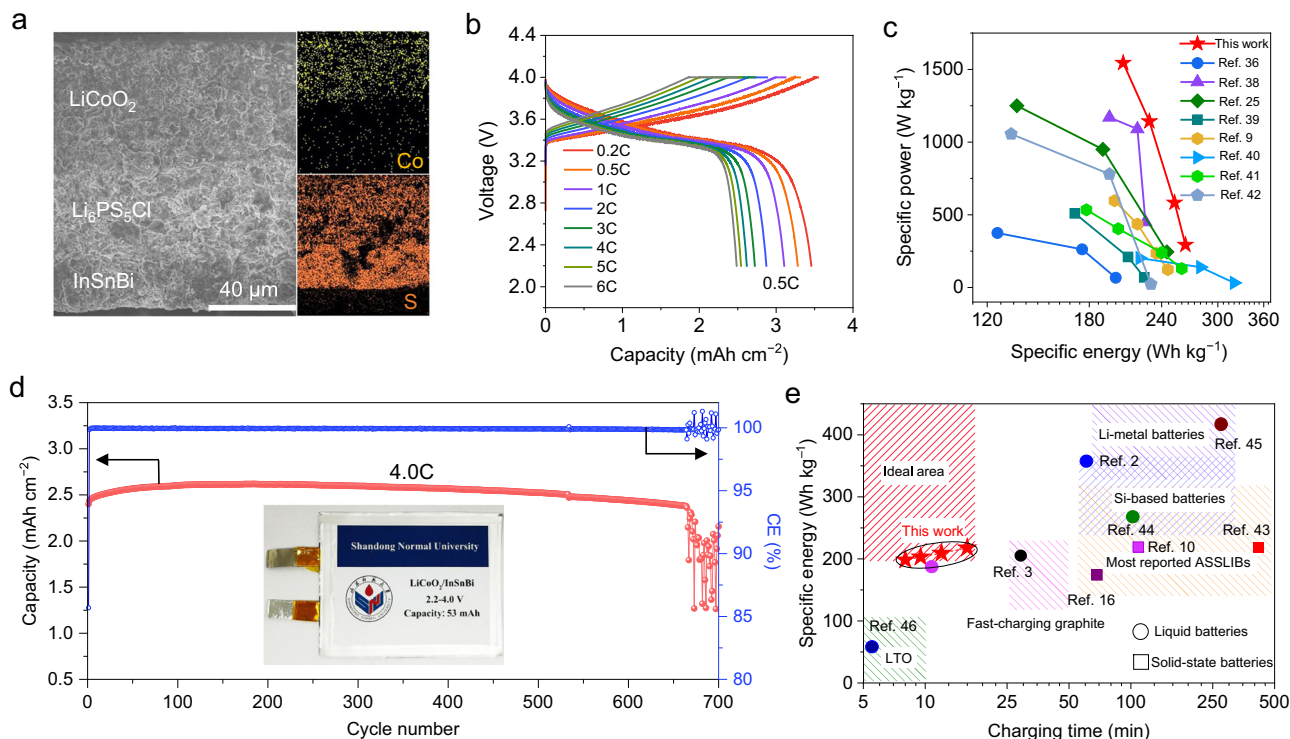


Fig. 6 | Electrochemical performance of full cells at 60 °C. a Cross-sectional SEM image of the initial InSnBi|LiPSCI|LiCoO₂ configuration. **b** Charging and discharging profiles of InSnBi || LiCoO₂ full-cell from 0.2 C to 6 C (with a fixed discharge rate of 0.5 C and a 3-min constant-voltage charging). **c** Comparison of the specific power of the InSnBi || LiCoO₂ cell with reported ASSLBs. **d** Cycling performance of our home-

made InSnBi || LiCoO₂ pouch cell (3.5 cm × 5.0 cm) at 4.0 C (The capacity of 53 mAh was measured at a rate of 0.2 C). **e** The comparison of fast-charging capability between our InSnBi || LiCoO₂ cell and representative publications. (LiCoO₂ based on 1 C = 145 mAh g⁻¹).

configuration, combining fast-charging capabilities with high-energy density, represents a great advancement compared to previous fast-charging batteries^{47–49}.

In this work, we demonstrate a rationally designed energy-dense planar alloy In_{0.38}Sn_{0.33}Bi_{0.29} that enables fast-charging capabilities in ASSLBs. The InSnBi alloy, comprising electrochemically reversible InBi-InSn₄ binary phases, exhibits highly MIEC percolation through its unique crystal-amorphous hybrid structure during cycling. This structural feature, coupled with stable chemo-mechanical compatibility with the LiPSCI solid electrolyte, effectively suppresses lithium dendrite formation during cycling, even under high areal capacities and current densities. In a full-cell configuration with a LiCoO₂ positive electrode, the ASSLB achieves a high specific energy of 278.4 Wh kg⁻¹ (919.5 Wh L⁻¹) at 0.2 C and sustains 73.6% and 72.0% of its specific energy with charging times of 9.5 min and 8 min, respectively. The straightforward synthesis of InSnBi negative electrodes, which requires only low-temperature heating (<100 °C) in air, presents great potential for commercial scale-up. These findings demonstrate the potential of InSnBi negative electrodes in realizing practical fast-charging, high-energy-density ASSLBs.

Methods

Materials preparation

Li₆PS₅Cl (6.8 mS cm⁻¹ at 25 °C) was obtained from Hefei Kejing Material Technology Co., Ltd. The alloy In_{0.38}Sn_{0.33}Bi_{0.29} was prepared by thoroughly mixing In (≥99.99%, Aladdin), Sn (≥99.5%, Aladdin), and Bi (≥99.99%, Aladdin) particles in an atomic ratio of 38:33:29, heating the mixture at 300 °C for 1 h under an argon atmosphere, and subsequently cooling it to room temperature in argon atmosphere. The InSnBi electrode was prepared as follows. The InSnBi alloy was melted in air using a tube furnace at 88 °C. The molten alloy was then uniformly spread onto the surface of a copper foil. The InSnBi-coated

copper foil was subsequently transferred onto a steel plate in contact with an ice–water mixture to facilitate rapid solidification of the alloy. After solidification, the InSnBi layer was repeatedly rolled using a rolling mill until the desired thickness was achieved. This method was also employed for preparing all other proportions of InSnBi alloys as well as for In₃Sn. 4.45 V high-voltage-type LiCoO₂ (LCO) was purchased from Guangdong Canrd New Energy Technology Co., Ltd. LiNi_{0.83}Co_{0.12}Mn_{0.05}O₂ (NCM83) positive electrode was obtained from RiseSun MGL Co., Ltd. Li₄Ti₅O₁₂ (D50 = 0.7–1.6 μm) was purchased from Dongguan Gelin Lithium Industry Co., Ltd.

LiPSCI film and electrode preparation

PTFE-LiPSCI film was fabricated by mixing 0.8 wt% PTFE and 99.2 wt% Li₆PS₅Cl powders by ball milling with 250 rpm for 15 min to ensure the fibrillation of PTFE. Then the obtained mixture was rolled to form a membrane with a loading of approximately 7.1 mg cm⁻². Subsequently, the film was cut into discs with a diameter of 10 mm. To prepared LCO electrodes for pouch cells, a mixture consisting of 73 wt% LCO, 15 wt% nm-LiPSCI, 10 wt% μm-LiPSCI, 2 wt% VGCF, and 0.8 wt% PTFE was initially blended to create a single flake. This flake was then subjected to repeated hot rolling to achieve the desired thickness before being punched into discs with dimensions of 35 × 50 mm for pouch cell assembly.

Cell and pouch cell fabrication

All the preparation processes were performed in an argon-filled glovebox (O₂ < 0.1 ppm, H₂O < 0.1 ppm). The fabrication of Li-InSnBi|LiPSCI|Li-InSnBi symmetric cell symmetric cells can be found in Supplementary Note 1. All-solid-state batteries employing InSnBi as negative electrodes were assembled as follows: Firstly, composite positive electrode powder (for rate performance) was prepared by mixing positive electrode materials (including LCO, NCM83 and LTO), LiPSCI

electrolyte, and VGCF with a weight ratio of 60:40:2 (LCO positive electrode), 55:45:5 (NCM83 positive electrode), and 30:60:10 (LTO positive electrode). Then, LiPSCI electrolyte (80 mg, Φ 10 mm) was pressed at 250 MPa for 3 min. After that, the composite positive electrode material was spread on one side of the LiPSCI electrolyte and pressed at 400 MPa for 3 min. InSnBi film (Φ 10 mm) was put on the other side of the LiPSCI, and in situ prelithiation was conducted by connecting InSnBi films and Li foils at 20 MPa for 120 min (Supplementary Note 3). After complete prelithiation, the full cell was pressed under a pressure of 100 MPa for 5 min. Unless otherwise specified, all cells were cycled under a pressure of 80 MPa. The pouch cell is assembled by stacking the composite positive electrode LCO, LiPSCI film, and InSnBi successively and is sealed in an aluminum-plastic bag. Then the pouch cell is clamped between two iron plates and tightened with screws with a pressure of 30 MPa during cycling.

Electrochemical measurements

Electrochemical impedance spectroscopy (EIS) measurements were performed on Li–InSnBi symmetric cells using an electrochemical workstation (VSP-300, Bio-Logic) over a frequency range from 7 MHz to 100 mHz, with six data points recorded per decade of frequency and an applied amplitude of 10 mV. The measurements were conducted at quasi-stationary potential by applying open-circuit voltage time longer than 30 min. EIS results were fitted using ZView software. Galvanostatic cycling tests were carried out under a stack pressure of 80 MPa using a Neware battery test system (CT-4008Q, China) at various current densities (LCO based on $1C = 145 \text{ mAh g}^{-1}$, NCM83 based on $1C = 180 \text{ mAh g}^{-1}$ and LTO based on $1C = 150 \text{ mAh g}^{-1}$). The liquid electrolyte used in Fig. 2f was a commercial electrolyte (1.0 M LiPF₆/EC-EMC (3:7, v/v)) purchased from Dodo Chemical Reagent Co., Ltd. All electrochemical tests were performed in a temperature-controlled chamber maintained at a constant temperature. A pulse current of 6 mA g^{-1} was applied for 20 min, with rest intervals of 1 h between each pulse. The diffusion coefficient (D_{Li^+}) can be estimated using the following generalized formula derived from Fick's second law.

$$D = \frac{4}{\pi\tau} \left(\frac{m_B V_m}{M_B S} \right)^2 \left(\frac{\Delta E_S}{\Delta E_\tau} \right)^2$$

Where τ is the current pulse duration in seconds, m_B denotes the active mass present in the sample, measured in grams, V_m and M_B refer to the molar volume and molar mass respectively, with units of cubic centimeters per mole and grams per mole, and S represents the active surface area of the electrodes, measured in square centimeters. Lastly, ΔE_S is the difference between the stable potentials, and ΔE_τ represents the instantaneous total voltage variation of the constant current battery at time τ . The values of ΔE_S and ΔE_τ can be derived from the Galvanostatic Intermittent Titration Technique (GITT) curves.

Materials characterization

Lab XRD measurements were carried out using a Rigaku SmartLab X-ray diffractometer with Cu K α radiation, with each XRD pattern recorded from 10° to 90° (step size of 0.01° and speed of 2.5° min⁻¹). In situ XRD was conducted on the liquid InSnBi/Li battery using an electrolyte of 1M LiFSI + hexyl methyl ether. The morphology, microstructure and elemental component of samples were carried out by a scanning electron microscopy (Hitachi S-4800, operated at 10 kV) and transmission electron microscopy (JEM 2100Plus, JEOL Limited Corporation, Japan). Cryo-SEM experiments were performed on a ThermoFisher Aquilos 2 Cryo-FIB system. SEM-EDS analysis was conducted with an energy cut-off of 15 kV at an ambient temperature of $24 \pm 1^\circ\text{C}$. During transfer into the sample chamber, the specimen was briefly exposed to ambient air. Following sample preparation, the specimen was transferred via a vacuum transfer vessel to a

Thermo Fisher ESCALAB 250Xi photoelectron spectrometer. All XPS spectra were acquired using a monochromatic Al K α X-ray source (1486.6 eV). The binding energy scale was calibrated by setting the adventitious carbon (C 1s) peak to 284.8 eV. Data analysis was subsequently performed using the XPSPEAK software. The DSC tests were performed on a differential scanning calorimeter (Q2000, TAinstrument) in Ar atmosphere at a scanning rate of 5°C min^{-1} from 20 to 250 °C. Raman measurements were performed using a HORIBA XploRA PLUS Raman spectrometer with a laser wavelength of 532 nm and a laser power of 3 mW. Hardness of different alloy negative electrodes were performed at the Nano Indenter G200 XP (Keysight) with a diamond Berkovich indenter. Young's modulus was investigated by atomic force microscopy (AFM, Bruker Multimode 8 with a Nanoscope V controller). The ⁷Li pulsed-field gradient (PFG) NMR experiments were performed on a Bruker AVANCE NEO 500WB spectrometer equipped with a Bruker Diff50 gradient probe, providing a maximum gradient strength of 1689 G/cm at 25 °C. Each sample was enclosed in a 5 mm quartz ampule under an inert atmosphere to prevent contamination. A pulse-gradient stimulated echo (PGSTE) sequence was employed for the ⁷Li nuclei. In this sequence, two identical magnetic field gradient pulses with amplitude G , a duration δ of 1.0 ms, and a diffusion delay Δ of 20 ms were applied following the first and third $\pi/2$ pulses. The In K-edge XAFS measurements were conducted at the BL14W beam line of the Shanghai Synchrotron Radiation Facility (SSRF, Shanghai, China), employing a Si (111) crystal monochromator. Prior to data collection, each sample was loaded into an aluminum holder and sealed with Kapton film to prevent contamination. The spectra were acquired at room temperature using a Bruker 5040 four-channel silicon drift detector (SDD). The In K-edge extended X-ray absorption fine structure (EXAFS) data were obtained in transmission mode. For each sample, two consecutive scans displayed consistent line shapes and edge positions in the XANES region, indicating reliable data quality. The standard reference samples were also measured in transmission mode. Data reduction and fitting were carried out with the Athena software package.

Computation

For the interface stability calculations, we treated the interface as a pseudobinary system composed of the two materials in contact, following the methodology outlined in previous work²⁴. This approach allows us to determine the set of phases with the lowest energy at any mixing ratio between the two phases. By representing this mixing ratio as a linear combination of the two parent phases normalized to one atom per formula unit, we can identify the phases that minimize the overall energy. The mutual reaction energy was determined by comparing the energy of the phase equilibria with the energy of the pseudobinary system at a specific mixing ratio, employing the same methodology as described in previous work²⁴.

First-principles calculations were performed within the plane-wave projector augmented wave (PAW) framework using the Vienna Ab initio Simulation Package (VASP)^{50,51} operated on the Medea platform. The exchange–correlation effects were treated using the generalized gradient approximation in the Perdew–Burke–Ernzerh form⁵². During the structural relaxations, a plane-wave cutoff energy of 520 eV was applied. Geometry optimization was carried out using the conjugate-gradient algorithm until the total energy and forces were converged to within 10^{-5} eV and 0.01 eV \AA^{-1} , respectively.

For the adhesion energy calculations, the corresponding calculation model and details are as follows:

In order to study the interfacial affinity of Li₃Bi, Li₁₃In₃ and Li₇Sn₂, the Li₃Bi(100)/Li₁₃In₃(001) and Li₃Bi(110)/Li₇Sn₂(010) interfacial supercell models were constructed. The interface properties such as interface formation energy E_f , interfacial energy σ and adhesion energy W_{ad} were calculated according to references^{53,54}.

The interfacial formation energy can be obtained by subtracting the energy of two stress-free pure phases with the same atomic number or minimum number of elements from the energy of the structurally relaxed interfacial phase. If the interfacial phase is composited with A (Li_3Bi) and B ($\text{Li}_{13}\text{In}_3$ or Li_7Sn_2), the interfacial formation energy E_f can be obtained by the following formula (1):

$$E_f = E_{A/B} - E_A^{\text{bulk}} - E_B^{\text{bulk}} \quad (1)$$

where $E_{A/B}$ is the energy after the interfacial supercell model is fully relaxed, E_A^{bulk} and E_B^{bulk} are the energies of the A part and B part under the state of no stress, respectively.

The interfacial energy σ can be calculated by the following formula (2):

$$\sigma = \left[E_{A/B} - E_A^{\text{bulk}(c)} - E_B^{\text{bulk}(c)} \right] / 2A \quad (2)$$

where $E_A^{\text{bulk}(c)}$ and $E_B^{\text{bulk}(c)}$ are the energies of the constrained bulks of A and B, that is, only axis C is relaxed while axis A and B are not relaxed. A is the area of the interface.

The work of adhesion W_{ad} can be calculated according to the following formula (3):

$$W_{\text{ad}} = \gamma_A + \gamma_B - \sigma_{A/B} \quad (3)$$

Where γ_A and γ_B are the surface energies of A and B in the interface model, respectively. The surface energy can be calculated by the following formula (4):

$$\gamma = (E_{\text{surf}} - nE_{\text{bulk}}) / 2S \quad (4)$$

where E_{surf} is the energy of the slab, E_{bulk} is the energy of the bulk structure, n is the number of unit in the slab, and S is the surface area of the slab.

The diffusion of Li^+ in the bulks of Li_3Bi , $\text{Li}_{13}\text{In}_3$ and Li_7Sn_2 was calculated by the climbing-image nudged elastic band (CI-NEB) method. In our AIMD simulations of Li_3Bi , Li_7Sn_2 and $\text{Li}_{13}\text{In}_3$, we employed defect-free crystal models rather than explicitly introducing vacancy defects, because the vacancy concentration in the actual crystal cannot be accurately determined by calculation or experiment. These coefficients should be understood as reflecting relative mobility trends rather than absolute values that would be observed in real materials with equilibrium defect concentrations.

COMSOL Multiphysics 5.4 is used to perform the modeling of lithiation uniformity of two negative electrode materials. In the modeling, the current distribution, mass transport, and electrochemical reactions coupled together.

Data availability

The authors declare that all the relevant data are available within the paper and its Supplementary Information file or from the corresponding author upon request. Source data are provided with this paper.

References

- Li, H. et al. Ampere-hour-scale soft-package potassium-ion hybrid capacitors enabling 6-minute fast-charging. *Nat. Commun.* **14**, 6407 (2023).
- Liu, T. et al. Recycled micro-sized silicon anode for high-voltage lithium-ion batteries. *Nat. Sustain.* **7**, 1057–1066 (2024).
- Han, J.-G. et al. An electrolyte additive capable of scavenging HF and PF5 enables fast charging of lithium-ion batteries in LiPF6-based electrolytes. *J. Power Sour.* **446**, 227366 (2020).
- Wang, C. Y. et al. Fast charging of energy-dense lithium-ion batteries. *Nature* **611**, 485–490 (2022).
- Tu, S. et al. Fast-charging capability of graphite-based lithium-ion batteries enabled by Li_3P -based crystalline solid-electrolyte interphase. *Nat. Energy* **8**, 1365–1374 (2023).
- Jin, H. et al. Black phosphorus composites with engineered interfaces for high-rate high-capacity lithium storage. *Science* **370**, 192–197 (2020).
- Kim, S. Y. & Li, J. Porous mixed ionic electronic conductor interlayers for solid-state batteries. *Energy Mater. Adv.* **2021**, 1519569 (2021).
- Li, M. et al. Dense all-electrochem-active electrodes for all-solid-state lithium batteries. *Adv. Mater.* **33**, e2008723 (2021).
- Lee, Y.-H. et al. Empowering all-solid-state Li-ion batteries with self-stabilizing Sn-based anodes. *Joule* **8**, 2777–2793 (2024).
- Wang, D. et al. Overcoming the conversion reaction limitation at three-phase interfaces using mixed conductors towards energy-dense solid-state Li-S batteries. *Nat. Mater.* **24**, 243–251 (2025).
- Duan, H. et al. Amorphous AlOCl compounds enabling nanocrystalline LiCl with abnormally high ionic conductivity. *J. Am. Chem. Soc.* **146**, 29335–29343 (2024).
- Sandoval, S. E. et al. Electro-chemo-mechanics of anode-free solid-state batteries. *Nat. Mater.* **24**, 673–681 (2025).
- Jeong, W. J. et al. Electrochemical behavior of elemental alloy anodes in solid-state batteries. *ACS Energy Lett.* **9**, 2554–2563 (2024).
- Yang, S. et al. In situ studies of lithium-ion diffusion in a lithium-rich thin film cathode by scanning probe microscopy techniques. *Phys. Chem. Chem. Phys.* **17**, 22235–22242 (2015).
- Chen, Z. et al. Large mechanical properties enhancement in ceramics through vacancy-mediated unit cell disturbance. *Nat. Commun.* **14**, 8387 (2023).
- Tan, D. H. S. et al. Carbon-free high-loading silicon anodes enabled by sulfide solid electrolytes. *Science* **373**, 1494–1499 (2021).
- Zheng, X. et al. High stability In-Sn-Bi multi-element alloy anode for Mg ion batteries. *J. Power Sour.* **575**, 233141 (2023).
- Mou, H. et al. Tin and Tin compound materials as anodes in lithium-ion and sodium-ion batteries: a review. *Front. Chem.* **8**, 141 (2020).
- Hänsel, C. et al. Favorable interfacial chemomechanics enables stable cycling of high-Li-content Li-In/Sn anodes in sulfide electrolyte-based solid-state batteries. *Chem. Mater.* **33**, 6029–6040 (2021).
- Xiong, X. et al. Creep-type all-solid-state cathode achieving long life. *Nat. Commun.* **15**, 3706 (2024).
- Zhang, B. B., Tang, Y. G., Mei, Q. S., Li, X. Y. & Lu, K. Inhibiting creep in nanograined alloys with stable grain boundary networks. *Science* **378**, 659–663 (2022).
- Degen, F., Winter, M., Bendig, D. & Tübke, J. Energy consumption of current and future production of lithium-ion and post lithium-ion battery cells. *Nat. Energy* **11**, 1284–1295 (2023).
- Luo, S. et al. Growth of lithium-indium dendrites in all-solid-state lithium-based batteries with sulfide electrolytes. *Nat. Commun.* **12**, 6968 (2021).
- Cao, D. et al. Stable thiophosphate-based all-solid-state lithium batteries through conformally interfacial nanocoating. *Nano Lett.* **20**, 1483–1490 (2020).
- Yan, W. L. et al. Hard-carbon-stabilized Li-Si anodes for high-performance all-solid-state Li-ion batteries. *Nat. Energy* **8**, 800–813 (2023).
- Li, Y. et al. A lithium superionic conductor for millimeter-thick battery electrode. *Science* **381**, 50–53 (2023).
- Wang, L. et al. Identifying the components of the solid-electrolyte interphase in Li-ion batteries. *Nat. Chem.* **11**, 789–796 (2019).

28. Wang, Y. et al. Facile design of sulfide-based all solid-state lithium metal battery: in situ polymerization within self-supported porous argyrodite skeleton. *Adv. Funct. Mater.* **31**, 2101523 (2021).
29. Langer, J., Epp, V., Heitjans, P., Mautner, F. A. & Wilkening, M. Lithium motion in the anode material LiC_6 as seen via time-domain ^7Li NMR. *Phys. Rev. B* **88**, 094304 (2013).
30. Mali, M., Roos, J., Sonderegger, M., Brinkmann, D. & Heitjans, P. ^6Li and ^7Li diffusion coefficients in solid lithium measured by the NMR pulsed field gradient technique. *J. Phys. F Met. Phys.* **18**, 403–412 (1988).
31. Sugiyama, J. et al. Li-ion diffusion in $\text{Li}_4\text{Ti}_5\text{O}_{12}$ and LiTi_2O_4 battery materials detected by muon spin spectroscopy. *Phys. Rev. B* **92**, 014417 (2015).
32. Ding, N. et al. Determination of the diffusion coefficient of lithium ions in nano-Si. *Solid State Ion.* **180**, 222–225 (2009).
33. Griffith, K. J., Wiaderek, K. M., Cibin, G., Marbella, L. E. & Grey, C. P. Niobium tungsten oxides for high-rate lithium-ion energy storage. *Nature* **559**, 556–563 (2018).
34. Kuhn, A., Duppel, V. & Lotsch, B. V. Tetragonal $\text{Li}_{10}\text{GeP}_2\text{S}_{12}$ and Li_7GePS_8 – exploring the Li ion dynamics in LGPS Li electrolytes. *Energy Environ. Sci.* **6**, 3548–3552 (2013).
35. Kuhn, A. et al. A new ultrafast superionic Li-conductor: ion dynamics in $\text{Li}_{11}\text{Si}_2\text{PS}_{12}$ and comparison with other tetragonal LGPS-type electrolytes. *Phys. Chem. Chem. Phys.* **16**, 14669–14674 (2014).
36. Wan, H., Wang, Z., Zhang, W., He, X. & Wang, C. Interface design for all-solid-state lithium batteries. *Nature* **623**, 739–744 (2023).
37. Wang, Y. T. et al. Self-organized hetero-nanodomains actuating super Li^+ conduction in glass ceramics. *Nat. Commun.* **14**, 669 (2023).
38. Ye, L., Lu, Y., Wang, Y., Li, J. & Li, X. Fast cycling of lithium metal in solid-state batteries by constriction-susceptible anode materials. *Nat. Mater.* **23**, 244–251 (2024).
39. Liu, Y. et al. Aluminum foil negative electrodes with multiphase microstructure for all-solid-state Li-ion batteries. *Nat. Commun.* **14**, 3975 (2023).
40. Zhang, Z. et al. Silicon-based all-solid-state batteries operating free from external pressure. *Nat. Commun.* **16**, 1013 (2025).
41. Shen, K. et al. All-solid-state batteries stabilized with electro-mechano-mediated phosphorus anodes. *Energy Environ. Sci.* **18**, 7568–7578 (2025).
42. Kim, C. et al. $\text{Nb}_{1.60}\text{Ti}_{0.32}\text{W}_{0.08}\text{O}_{5-8}$ as negative electrode active material for durable and fast-charging all-solid-state Li-ion batteries. *Nat. Commun.* **15**, 8832 (2024).
43. Lu, P. et al. Realizing long-cycling all-solid-state $\text{Li-In}|\text{TiS}_2$ batteries using $\text{Li}_{6+x}\text{M}_x\text{As}_{1-x}\text{S}_5\text{I}$ ($\text{M}=\text{Si}, \text{Sn}$) sulfide solid electrolytes. *Nat. Commun.* **14**, 4077 (2023).
44. Ko, S. et al. Electrolyte design for lithium-ion batteries with a cobalt-free cathode and silicon oxide anode. *Nat. Sustain.* **6**, 1705–1714 (2023).
45. Zhang, Q.-K. et al. Homogeneous and mechanically stable solid–electrolyte interphase enabled by trioxane-modulated electrolytes for lithium metal batteries. *Nat. Energy* **8**, 725–735 (2023).
46. Zaghbi, K. et al. Safe and fast-charging Li-ion battery with long shelf life for power applications. *J. Power Sour.* **196**, 3949–3954 (2011).
47. Lee, S. M. et al. A cooperative biphasic $\text{MoO}(x)\text{-MoP}(x)$ promoter enables a fast-charging lithium-ion battery. *Nat. Commun.* **12**, 39 (2021).
48. Chakraborty, P. et al. Addressing the range anxiety of battery electric vehicles with charging en route. *Sci. Rep.* **12**, 5588 (2022).
49. Weiss, M. et al. Fast charging of lithium-ion batteries: a review of materials aspects. *Adv. Energy Mater.* **11**, 33 (2021).
50. Kresse, G. et al. Ab initio molecular-dynamics simulation of the liquid-metal–amorphous-semiconductor transition in germanium. *Phys. Rev. B* **49**, 14251–14269 (1994).
51. Kresse, G. et al. Efficiency of ab-initio total energy calculations for metals and semiconductors using a plane-wave basis set. *Comput. Mater. Sci.* **6**, 15–50 (1996).
52. Perdew, J. P., Burke, K. & Ernzerhof, M. Generalized Gradient Approximation Made Simple. *Phys. Rev. Lett.* **77**, 3865–3868 (1996).
53. Hu, A. et al. An artificial hybrid interphase for an ultrahigh-rate and practical lithium metal anode. *Energy Environ. Sci.* **14**, 4115–4124 (2021).
54. Li, W. et al. $\text{SnF}(2)$ -Catalyzed Formation of Polymerized Dioxolane as Solid Electrolyte and its Thermal Decomposition Behavior. *Angew. Chem. Int. Ed. Engl.* **61**, e202114805 (2022).

Acknowledgements

This work was financially supported by the National Key R&D Program of China (Grant No. 2023YFC2812700, received by G.C.), the Key Scientific and Technological Innovation Project of Shandong (Grant No. 2022CXGC020301, received by G.C.), the National Natural Science Foundation of China (Grant No. U22A20440, received by G.C.; Grant No. 22209195, received by T.L.; Grant No. 22139001, received by G.C.), Natural Science Foundation of Shandong Province (Grant No. ZR2022QB172, received by T.L.), and supported by Shandong Energy Institute. The authors are grateful to the Instrumental Analysis Center of Xi'an Jiaotong University and Xiaohua Cheng at the Center for Advancing Materials Performance from the Nanoscale (CAMP-Nano) in Xi'an Jiaotong University for characterizations.

Author contributions

T.L. and G.C. conceived the idea for this project. T.L., Y.S., and Y.W. prepared the materials and carried out electrochemical tests and characterizations. S.Z. conducted the simulations. Y.Z. and J.W. performed the ^7Li PFG NMR spectroscopy. We would like to acknowledge the discussion with Prof. Evan Ma and his insightful perspectives. S.D., C.L., L.H., W.X., J.J., J.M., and B.T. discussed together and proposed the concepts of this paper. All authors participated in manuscript preparation.

Competing interests

The authors declare no competing interests.

Additional information

Supplementary information The online version contains supplementary material available at <https://doi.org/10.1038/s41467-025-67352-w>.

Correspondence and requests for materials should be addressed to Shanmu Dong, Weijiang Xue, Bo Tang or Guanglei Cui.

Peer review information *Nature Communications* thanks Lingyun Zhu, and the other, anonymous, reviewer(s) for their contribution to the peer review of this work. A peer review file is available.

Reprints and permissions information is available at <http://www.nature.com/reprints>

Publisher's note Springer Nature remains neutral with regard to jurisdictional claims in published maps and institutional affiliations.

Open Access This article is licensed under a Creative Commons Attribution-NonCommercial-NoDerivatives 4.0 International License, which permits any non-commercial use, sharing, distribution and reproduction in any medium or format, as long as you give appropriate credit to the original author(s) and the source, provide a link to the Creative Commons licence, and indicate if you modified the licensed material. You do not have permission under this licence to share adapted material derived from this article or parts of it. The images or other third party material in this article are included in the article's Creative Commons licence, unless indicated otherwise in a credit line to the material. If material is not included in the article's Creative Commons licence and your intended use is not permitted by statutory regulation or exceeds the permitted use, you will need to obtain permission directly from the copyright holder. To view a copy of this licence, visit <http://creativecommons.org/licenses/by-nc-nd/4.0/>.

© The Author(s) 2025